Earth and Planetary Science Letters 578 (2022) 117296

Contents lists available at ScienceDirect

Earth and Planetary Science Letters

www.elsevier.com/locate/epsl

Hypocentral dependent shallow slip distribution and rupture extents along a strike-slip fault

Suli Yao, Hongfeng Yang *

Earth System Science Programme, The Chinese University of Hong Kong, Shatin, Hong Kong, China

ARTICLE INFO

Article history:
Received 6 July 2021
Received in revised form 24 October 2021
Accepted 10 November 2021
Available online 18 November 2021
Editor: J.-P. Avouac

Keywords:
dynamic rupture scenarios
Anninghe fault
interseismic locking
surface rupture
shallow slip deficit

ABSTRACT

Natural faults feature heterogeneities in geometry, material properties, and stress distributions, posing great challenges in predicting fault slip behaviors. Among these factors, the stress on the fault is poorly understood due to the lack of direct measurements. Here, we estimate stress distribution from interseismic locking models and derive earthquake scenarios along the Anninghe fault in Sichuan, China, by conducting dynamic rupture simulations. The predicted rupture segmentation and moment magnitudes (Mw 6.9 – 7.3) are well consistent with historical earthquakes. Besides, we have observed models accompanied by continuous surface rupture, with surface offsets comparable to the values identified in field surveys of historical earthquakes. In addition, the surface rupture and the shallow slip deficit (SSD) vary drastically among models with different hypocenters, demonstrating that the earthquake process is indeterministic. The coseismic moment predicted in our models is ~50% of what was anticipated from the static locking model. Our results highlight that those rupture scenarios derived from the locking-based heterogeneous stress can further contribute to the seismic hazard assessment.

1. Introduction

Assessment of earthquake hazards along continental strike-slip faults is highly demanded, particularly in densely populated areas. In addition to earthquake magnitude and rupture extent, whether the rupture may break the ground and/or large slip may occur near the surface plays a key role in controlling ground motion intensities in continental strike-slip earthquakes (Pitarka et al., 2009). Although most earthquakes are buried (Biggs et al., 2006) or leave a substantial shallow slip deficit (SSD: near-surface slip is usually much smaller than the maximum slip at greater depths) (Fialko et al., 2005), some exceptions apparently do not host obvious SSD and are thus very destructive, such as the 2010 Qinghai Yushu Mw 6.9 and the 2014 Yunnan Ludian Mw 6.1 earthquakes (Yang and Yao, 2021). The mechanism controlling SSD has been attributed to the coseismic plastic deformation of the shallow compliant fault zone (Kaneko and Fialko, 2011; Roten et al., 2017). However, a shallow compliant zone may not always reduce slip at shallow depths (Weng et al., 2016). It has also been reported that the apparent SSD is mainly due to the neglect of spatial variations in elastic modulus especially for the shallow compliant zone (Barbot et al., 2008, 2009) and the insufficient near-fault coseismic deformation data coverage (Xu et al., 2016) in the slip inversion process. Evaluating the potential of surface-breaching rupture and investigating the factors that control the shallow slip along continental faults are critical in seismic hazard assessment.

Fault zones are complex systems with a variety of heterogeneities in geometry, material properties, and stress conditions (Lindsey and Fialko, 2013; Lei and Zhao, 2009; H. Yang et al., 2011; Goebel et al., 2012), all of which were well known to impact earthquake nucleation and rupture propagation. For instance, the material contrast across the fault may give rise to a preferential rupture directivity (Andrews and Ben-Zion, 1997). Besides, irregular fault geometry, such as a bend, a bump, or a jump, has been evidenced to be responsible for rupture initiation and termination (King and Nábělek, 1985; Elliott et al., 2015; Yang et al., 2012, 2013). Despite impacts from the structure, fault slip is indeed controlled by the competition between the shear stress and the frictional resistance (strength). Although the stress and the strength levels on seismogenic faults remain elusive, a variety of evidence suggests that they are quite heterogeneous on faults, such as microseismicity in fault transition zones (Jiang and Fialko, 2016), neighboring creeping or locked segments (Wyss, 2001; Fournier and Freymueller, 2007), complex slip and stress drop patterns in large earthquakes (Xu et al., 2010; Shrivastava et al., 2016), and interseismic locking models (Noda et al., 2018; McCaffrey, 2014). There is no doubt that the

* Corresponding author.
E-mail address: hyang@cuhk.edu.hk (H. Yang).

https://doi.org/10.1016/j.epsl.2021.117296
0012-821X/

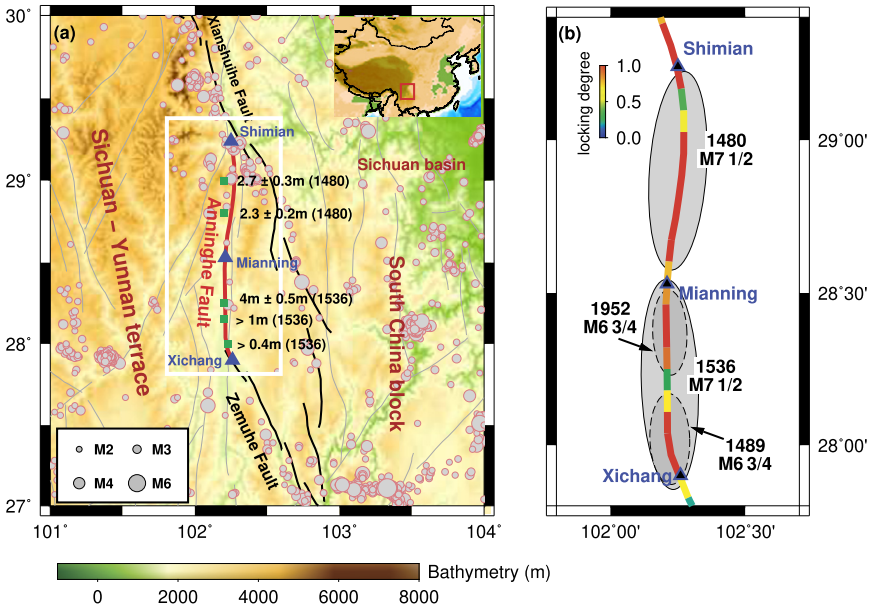

Fig. 1. (a) Map for the Anninghe fault region. The thick red line indicates the trace for the Anninghe fault (Deng et al., 2003). The green squares are the locations of identified surface slip in the field for historical earthquakes (Yu et al., 2001; Wen et al., 2000, 2007). The gray dots are seismicity with magnitudes over 2 since 2008, provided by Data Sharing Infrastructure of National Earthquake Data Center (http://data.earthquake.cn). (b) Historical earthquakes (Wen, Ma et al., 2008) and the locking degree (Jiang et al., 2015) along the Anninghe fault. (For interpretation of the colors in the figure(s), the reader is referred to the web version of this article.)

stress patterns on faults largely determine the location, the extent, and the rupture process of future earthquakes (Yang et al., 2019a; Harris, 2004). However, unlike the fault structure that can be explored through seismic imaging, stress patterns on faults are poorly understood due to the lack of direct measurements. In earthquake simulations, the initial stress is commonly assumed to be uniform, depth-dependent, or stochastic (Olsen et al., 2006; Ripperger et al., 2008; Bydlon et al., 2019). Recently, interseismic locking distribution has been used to estimate initial stress distribution (Yang et al., 2019a; Li and Liu, 2021; Ramos et al., 2021; Noda et al., 2021; Harris et al., 2021), giving a viable approach to develop physics-based rupture scenarios.

We investigate the seismic potential along the Anninghe fault, which is located at the eastern boundary of the Tibetan Plateau. The Anninghe fault is a sinistral strike-slip fault that extends ~150 km along strike from Shimian in the north to Xichang in the south. The Anninghe fault has been identified as a seismic gap that had hosted M7 earthquakes with recurrence intervals around 400-600 yrs (Wen et al., 2008; Wen, Ma et al., 2008; Ran et al., 2008). The latest large event occurred in 1536 (M $7\frac{1}{2}$) (Fig. 1) (Wen, Ma et al., 2008). Therefore, the Anninghe fault is in the late phase of the interseismic period. Moreover, both the extremely low seismicity and the high interseismic locking degree (Jiang et al., 2015) indicate that the Anninghe fault has been accumulating elastic potential energy (Fig. 1 & 2a). Besides, evidence from the field indicates significant surface slip up to 4 m caused by historical earthquakes along the Anninghe fault, suggesting potential surface rupture in future earthquakes (Yu et al., 2001; Wen et al., 2000, 2007) (Fig. 1a).

Here, we conduct dynamic rupture simulations to investigate potential scenarios for future earthquakes along the Anninghe fault. We involve heterogeneities in stress on the fault with the constraint from an interseismic locking model (Yang et al., 2019a,b). We then nucleate ruptures from different locations and analyze the earthquake magnitude, the rupture extent, and the potential of surface rupture along the Anninghe fault. Furthermore, we compare our model predictions with the historical earthquakes.

2. Method and model setup

2.1. 3-D fault model setup

We construct a 3-D cubic elastic model for the Anninghe fault, which extends 210 km along-strike, 100 km in the strike-normal direction, and 50 km at depth. The fault trace is from Deng et al. (2003). According to the deep seismic sounding profiles (Z. Yang et al., 2011), the Anninghe fault dips to the east with an angle of 80°-90°. We simplify the fault geometry by assuming a vertical fault plane. The geographical reference point of our model is at (102.0, 27.8). We extract a 1-D depth-dependent velocity model for the Anninghe region and adopt it to prescribe material properties (Table S1) (Yang et al., 2020). To meet the numerical requirements, the grid size is 150 m on the fault (See details in supplementary materials, Fig. S1). On the ground surface, the grid size gradually increases from 150 m on the fault trace to 3 km on the boundaries.

2.2. Calculation for interseismic stress accumulation and initial stress

The initial stress, as a key ingredient in dynamic rupture simulations, is calculated based on an interseismic locking model that was derived from GPS and InSAR data (Jiang et al., 2015), following the approach in Yang et al. (2019a). The slip deficit rate on the Anninghe fault is ~10 mm/yr with a locking depth of ~15 km (Jiang et al., 2015). Since the latest two M7 events occurred in 1536 on the southern portion and in 1480 on the northern segment (Fig. 1), we assume an interseismic accumulation period of 500 years. Based on the calculation results, the max stress build-up on the Anninghe fault is ~ 25 MPa (Fig. 2b). Our calculation result indicates three high-stress asperities along the Anninghe fault (Fig. 2b). The largest one is located in the northern part extending from Shimian to Mianning with a length of ~50 km (M3). The other two reside in the south with lengths around 20 km (M2) and 30 km (M1), respectively. The initial shear stress is given by a superposition of the stress accumulated during the interseismic period and a constant dynamic stress (τ_d, i.e. 30 MPa). The effective normal stress on the fault is 100 MPa.

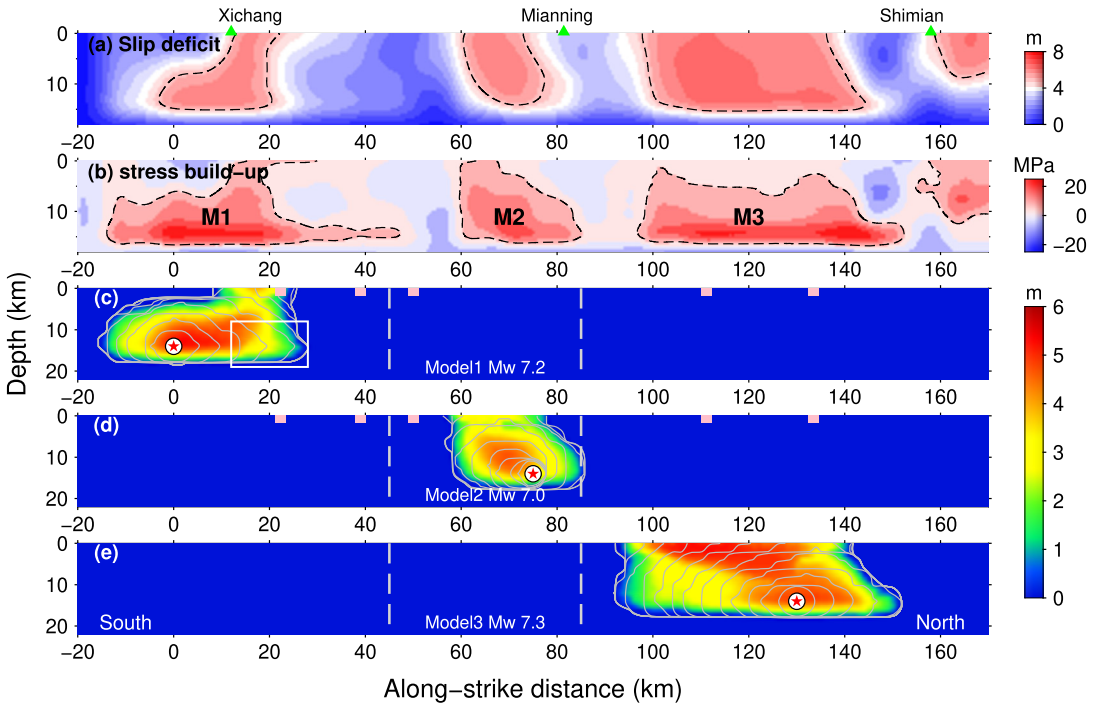

Fig. 2. (a) Total slip deficit on the Anninghe fault by assuming an interseismic period of 500 yrs. (b) Stress build-up on the fault caused by the slip deficit in (a). (c), (d), (e) Final slip distribution of dynamic rupture models on three segments. The red stars denote the hypocenters. The thin gray contours are the rupture fronts every second. The thick gray dashed lines indicate the locations of segmentation in historical earthquakes (Wen, Ma et al., 2008). The pink squares stand for the sites with surface slip identified in the field (Yu et al., 2001; Wen et al., 2000, 2007). The white box in panel (c) indicates the region with supershear rupture speed.

2.3. Frictional parameters in dynamic rupture models

We adopt a linear slip-weakening law as the constitutive law (Ida, 1972) on the fault in dynamic rupture simulations. In this friction law, the frictional strength linearly decreases from the yield stress (τ_s) to the dynamic stress (τ_d) with slip increasing from zero to the critical weakening distance (D_c). Due to the lack of prior knowledge of frictional properties on the fault, we set the frictional parameters to be uniform on the fault. The τ_d and τ_s are assumed to be 30 MPa and 60 MPa, respectively.

Seismic observations have suggested that the critical weakening distance scales with the final slip (Viesca and Garagash, 2015; Cocco et al., 2009), which is predicted by the thermal-pressurization mechanism (Viesca and Garagash, 2015; Rice, 2006). The scaling factor is around 0.1-0.2 (Yao and Yang, 2020; Weng and Yang, 2018). As such, a Dc of 0.6 m is reasonable for M7 earthquakes. Nevertheless, the weakening distance scatters from 0.1 to 10 m and might drop down to the millimeter scale in fast-sliding friction experiments of vast types of rock samples under different effective normal stress, different slip rates, and different hydro-thermal conditions (Kuo et al., 2013; Di Toro et al., 2011). For instance, the critical weakening distance decreases with the effective normal stress as the heating efficiency increases (Yao et al., 2013; Di Toro et al., 2011). However, the frictional parameters measured in lab may not be consistent with those estimated from seismic observations potentially due to the different weakening mechanisms (Nielsen et al., 2016). For instance, such experiments do not involve the influence of fault structure such as the fluid migration in the fracture network. Here, we adopt a Dc of 0.6 m by referring to the estimate of Dc from seismic observations.

Frictional parameters, including the differences between the yield stress (τ_s), the dynamic stress (τ_d), and the initial stress (τ_i), as well as the critical weakening distance Dc, play critical roles in controlling rupture propagation. Transitions of dynamic rupture types are expected if a broad range of frictional parameters is explored (Gabriel et al., 2012; Xu et al., 2015). For instance, decreasing the Dc or the yield stress can accelerate ruptures and may cause the transition from self-arresting to subshear or even to supershear ruptures. The fracture energy, which is the energy required for the rupture fronts to propagate, calculated as $G_c = 0.5 * D_c * (\tau_s - \tau_d)$, is $9.0 \times 10^6 J/m^2$ in our models, residing in the range estimated from seismic observations (Viesca and Garagash, 2015) for an average slip of 2.5 m. As there are no independent constraints on the frictional properties on the Anninghe fault, we discuss the influence of those frictional parameters in section 3.3.

2.4. Earthquake nucleation

We nucleate ruptures by decreasing the strength to be 0.01 MPa lower than the average initial stress in the nucleation zones. Considering that large earthquakes usually initiate from the deep bound of the seismogenic zones (Das and Scholz, 1983), we nucleate ruptures at the depth of 14 km. In general, the nucleation size should be as small as possible to minimize artificial effects (Galis et al., 2015). Here, we set the nucleation radius to be 2 km. The model results with nucleation radii of 2 km and 3 km are very consistent, indicating that the impact from the nucleation size on the model result is negligible (Fig. S2). The time step of dynamic rupture simulations is 0.005 s. We use a finite element package PyLith (Aagaard et al., 2013) to conduct the dynamic rupture simulations.

3. Results

3.1. Predicted earthquake magnitude and rupture extent along the Anninghe fault

By adopting different nucleation sites, we yield rupture scenarios with magnitudes ranging from Mw 7.0 – 7.3. Among these scenarios, the max fault slip is around 4-6 m, with an average rupture

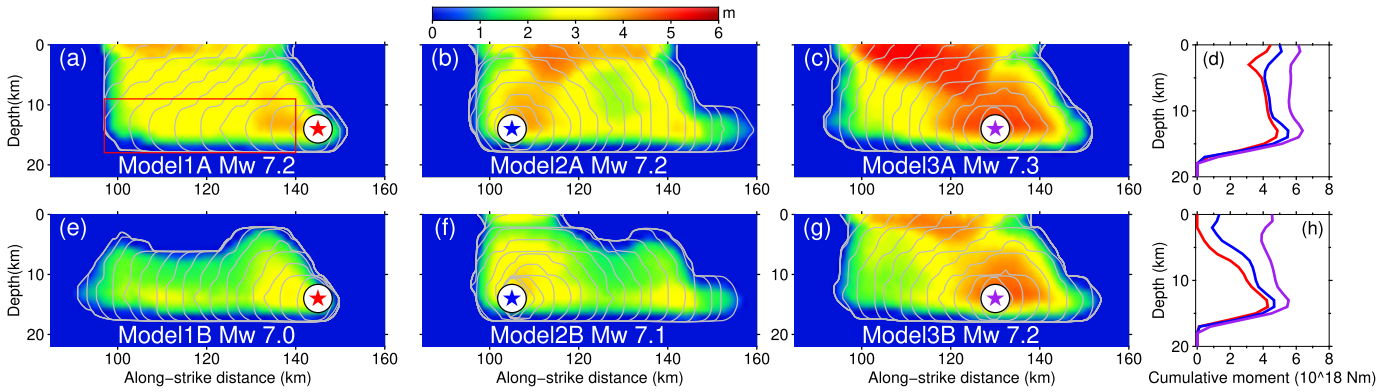

Fig. 3. Final slip distribution in dynamic rupture models at the northernmost segment (M3) with different nucleation sites. The yield stress (τ_s) is 60 MPa in models 1A-3A (a), (b), (c) and is 65 MPa in models 1B-3B (e), (f), (g). The stars indicate the hypocenter locations. The thin gray contours are the rupture fronts every second. The red box in panel (a) indicates the area with supershear rupture speed. Panel (d) and (h) show the cumulative moment versus depth in models 1A-3A and 1B-3B, respectively.

speed of ∼3 – 3.5 km/s. Due to the high stress at the down-dip locking edge (Fig. 2b), ruptures propagate with supershear rupture speed on some portions at depth. However, ruptures always terminate at the two gaps between asperities (Fig. 2c-e), resulting from the lack of strain energy to overcome the fracture energy in the low-stress regions. In addition, our models neglect the negative stress perturbation on segment M2 caused by the most recent large event in 1952 (M $6\frac{3}{4}$), which is supposed to enhance rupture segmentations. Based on our modeling results, we propose that the present stress barriers between the asperities are strong, thus it is unlikely to have ruptures going through the entire Anninghe fault.

Our model predictions are well consistent with historical earthquakes in the locations of rupture extents and earthquake magnitudes (Fig. 2). Based on field observations and ground motion intensity reports, no historical earthquakes or paleoearthquakes were believed to have ruptured the entire Anninghe fault at once (Wen, Ma et al., 2008; Yu et al., 2001; Wen et al., 2000, 2007). The 1480 (M $7\frac{1}{2}$) and the 1536 (M $7\frac{1}{2}$) earthquakes were inferred to be segmented at Mianning, while the 1489 (M $6\frac{3}{4}$) and the 1952 (M $6\frac{3}{4}$) were inferred to terminate at the middle way between Mianning and Xichang (Wen, Ma et al., 2008). The magnitudes of the historical earthquakes on the Anninghe fault range from M $6\frac{3}{4}$ to $7\frac{1}{2}$, which were derived based on the empirical relationship between the rupture length and the magnitude (Wen, Ma et al., 2008). The consistency between model predictions and historical earthquakes highlights the reliability of the locking-based scenarios.

3.2. Hypocentral effects on potential surface rupture and SSD

In addition to the magnitude and the rupture extent, the surface rupture and the shallow slip are critical in hazard risk assessment. In our models, we observe continuous surface rupture with large offsets, as well as considerable shallow slip along the northernmost (M3) segment. The amount of surface slip (2–5 m) is comparable to the estimations in historical earthquakes (Yu et al., 2001; Wen et al., 2000, 2007). In contrast, surface rupture is minor on another two segments in the south, where the extent of the surface rupture is up to 12 km (Fig. 2). As a result, the SSD is significant in rupture models on the two segments in the south. Most of the sites with surface slip identified in the field reside in our predicted surface-breaching region (Fig. 2), except two sites near the middle way between Mianning and Xichang that were caused by the 1480 M$7\frac{1}{2}$ earthquake. The reason is due to the absence of rupture models through the entire southern segment.

In addition, the shallow slip pattern varies among ruptures nucleated from different locations. For instance, we nucleate a rupture near Shimian in the north (model 1A) which finally breaks the surface with surface slip around 3 m and a moment magnitude of 7.2 (Fig. 3a). In comparison, the rupture nucleated from the middle of the segment results in surface slip up to 5 m with a higher moment magnitude of 7.3 (model 3A, Fig. 3c). Another case (model 2A, Fig. 3b) initiated from the southern part of M3 results in moderate surface slip compared to the above two cases. Due to such hypocenter-dependent effects, SSD in our models varies from 0 – 20% among ruptures on M3. The hypocenter-dependent effect is minor on segments M1 and M2 mainly due to the limited surface rupture extent and heterogeneities inside (Fig. S3).

Such hypocenter-dependent effects arise from the heterogeneous stress distribution and consequent different energy release processes in earthquakes nucleated from different sites. Here, we estimate the available energy, which is defined as the difference between the total elastic strain energy release and the frictional energy, as an index for the energy release rate (Noda et al., 2021). It is calculated as $\iint \frac{1}{2}(\Delta\sigma \times D)\,dS$, where $\Delta\sigma$ is stress drop and D is fault slip. We find that the release rates in models 1A and 3A are higher than the model 2A at the initial stage (0–3 s), due to the difference in initial stress inside and near the nucleation zones (Fig. 4a). Then in the later stage, model 3A grows much faster than the other two as a bi-lateral rupture, leading to a more energetic rupture front when reaching the surface (Fig. S4 & S5). The strong reflection phases and the mirror effect, as well as the systematic change of the shape factor scaling between stress drop and slip when the free surface is broken, enhance the shallow slip in model 3A (Shimazaki, 1986; Kaneko and Lapusta, 2010). Another potential explanation for the difference in shallow slip is due to the shape of the rupture front. In model 3A, the rupture goes directly upward to the surface, resulting in significant overlap and interaction between the rupture front and the reflection phases. Hence, the amplification on shallow slip due to the free surface effect is more significant in model 3A (Fig. S4 & S5).

3.3. Dependency on the frictional properties

Here, we test the dependency of model results on frictional parameters. We first test models by increasing the yield stress (τ_s) to 65 MPa. Such change depresses the rupture propagation and the energy release. The rupture speed drops to subshear in all models (Fig. 3e-g). The available energy drops by ∼20% compared to models with τ_s of 60 MPa (Fig. 4b). Although the rupture process changes, all models remain segmented at the two low-stress gaps with moment magnitudes from 7.0 to 7.2 (Fig. S6). In addition, as the rupture is depressed compared to the previous parameter settings, we have observed buried ruptures due to the lack of strain energy to break the shallow portion (Fig. 3e), while the surface-

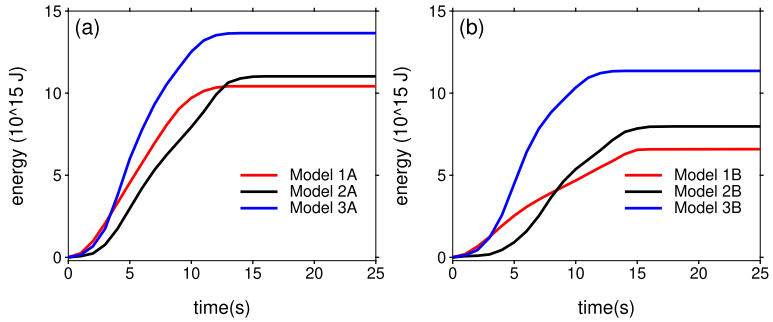

Fig. 4. Evolution of the available energy over time in rupture models in Fig. 3.

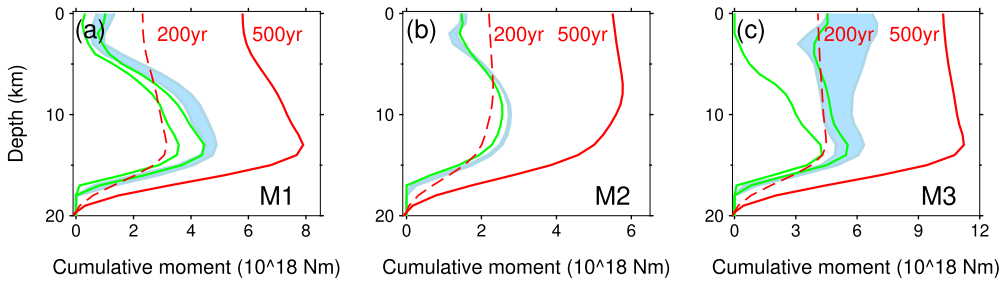

Fig. 5. Comparison in the predicted moment release between our dynamic models and the static interseismic locking models (red solid lines: an interseismic period of 500 yrs; red dashed lines: 200 yrs). The blue shadows indicate the predictions in models with τ_s of 60 MPa and Dc of 0.6 m. The green lines indicate the bounds of the predictions in models with τ_s of 65 MPa and Dc of 0.6 m. Only one breakaway case with τ_s of 65 MPa and Dc of 0.6 m is obtained on M2, plotted as the green line in panel (b). Three panels indicate three segments: (a) for the southernmost segment, (b) for the middle segment, and (c) for the northernmost segment.

breaching cases still exist (Fig. 3f & 3g). As a result, the SSD scatters from 0 to 100% among rupture models on M3 (Fig. 5).

In addition, we test models by increasing Dc to 0.8 m. Similarly, ruptures are depressed and some even turn into self-arresting (Fig. S8). We further test models by decreasing the yield stress to 56 MPa, 1.5 MPa higher than the maximum of the initial stress. Such a decrease accelerates all ruptures on M1 and M3 to supershear rupture speed (Fig. S7). Although the rupture mode changes, the segmentation and the hypocenter-dependent effects still exist (Fig. S6–S9). The model results indicate that the hypocenter-dependent effect is a natural outcome of the heterogeneous stress under different rupture types.

4. Discussion

4.1. Implications on surface rupture behaviors and SSD mechanism

We attribute the hypocenter-dependent shallow slip behaviors to the heterogeneous stress on the fault. Different hypocenters lead to different kinetic energy at the rupture fronts, which can influence the rupture propagation at the shallow depth and the interaction between the rupture and the free surface (Yang et al., 2019b). Historical earthquakes along the Anninghe likely feature such variations. For instance, significant surface slip up to 4 m caused by two M $7\frac{1}{2}$ events in 1480 and 1536 has been reported (Yu et al., 2001; Wen et al., 2000, 2007) (Fig. 1a). However, for the 1489 M $6\frac{3}{4}$ earthquake, and the most recent M $6\frac{3}{4}$ earthquake in 1952, no surface slip has been found.

The main reason responsible for SSD in our models is that the material at the shallow depth is weak hence the stress build-up is lower compared to the deep portion, which may suppress ruptures at shallow depths (Fig. 2b). Our model results indicate that the SSD may naturally vary in a large range due to the indeterministic rupture process under a heterogeneous stress condition, which serves as a new mechanism to explain observed different SSDs under similar tectonic settings.

4.2. Moment release in static and dynamic rupture scenarios

The interseismic locking models derived from geodetic observations have been widely applied in earthquake potential assessment (Tymofyeyeva and Fialko, 2018; Ader et al., 2012). In static scenarios, a complete release of the slip deficit in future earthquakes are commonly assumed (e.g. Baranes et al., 2018; Jiang et al., 2015). Here, we examine the difference between the predictions on moment release from the dynamic rupture simulations and the static estimations. We find that the moments in our dynamic models approximate 50% of the static predictions. The max slip in the dynamic models is $\sim$ 5 m, about 67% of the max slip deficit (i.e. 7.5 m). Such overprediction from static locking models has been evidenced in observations. For instance, the Mw 7.6 2012 Nicoya earthquake broke part of the identified locked patches with a magnitude smaller than the anticipated value (i.e. Mw 7.8) (Feng et al., 2012; Protti et al., 2014). Similarly, incomplete slip deficit release has been reported in the 2015 Nepal Mw 7.8 earthquake (Li et al., 2016) and the 2010 Maule Mw 8.8 earthquake (Moreno et al., 2010).

A viable explanation is that regions with low to moderate locking degrees usually host little slip or remain unbroken in dynamic rupture scenarios, while they all contribute to the static predictions. Due to the source scaling law that the slip increases with the rupture extent under the same stress drop, such a decrease in the rupture area limits the slip in the dynamic models. Such comparison together with the rupture segmentation highlights the necessity of dynamic rupture models in addition to the static locking models in seismic risk assessment.

4.3. Synthetic ground motions and implications on seismic hazard assessment

Earthquakes cause severe damage by generating strong ground shaking. In addition to rupture scenarios, we simulate the ground motions for the region within 50 km from the fault trace. To

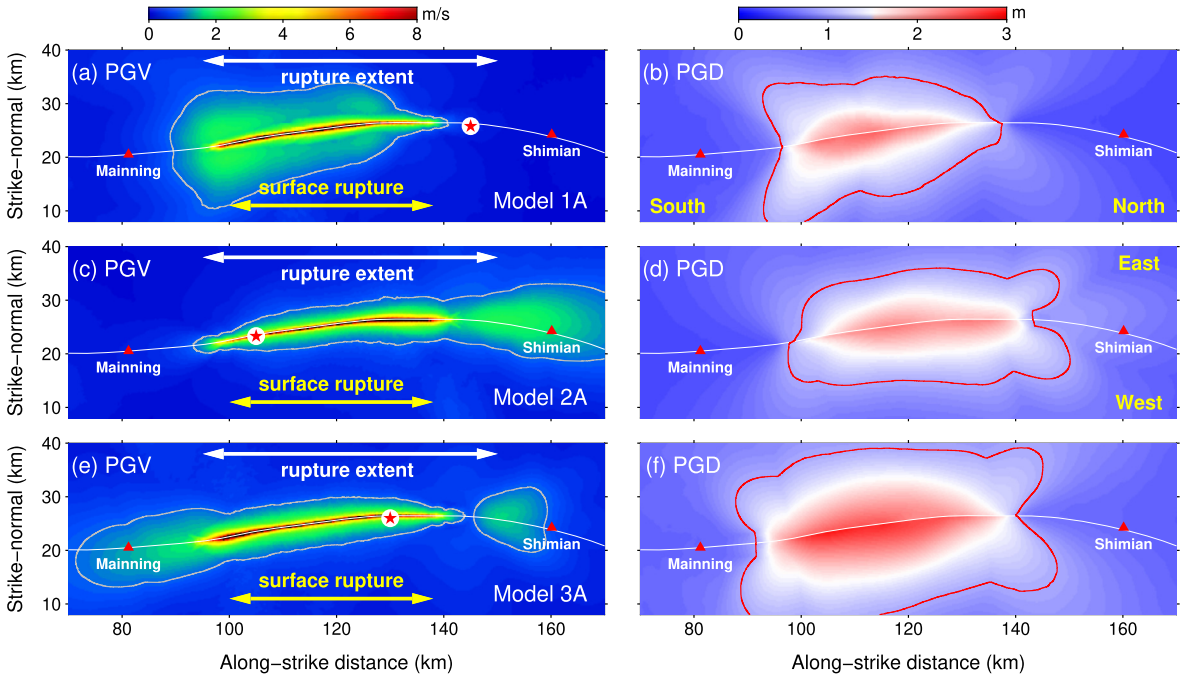

Fig. 6. Ground motion intensities in rupture models 1A-3A in Fig. 3. Panels (a) and (b) are for the model 1A in Fig. 3; (c) and (d) for model 2A; (e) and (f) for model 3A. Panels (a), (c), and (e) show the distribution of the peak ground velocity (PGV), while (b), (d), and (f) represent the spatial patterns of the peak ground displacement (PGD). The contours indicate the PGV of 1 m/s in (a), (c), and (e) and the PGD of 1 m in (b), (d), and (f), respectively. The red triangles denote the locations of cities near the Anninghe fault.

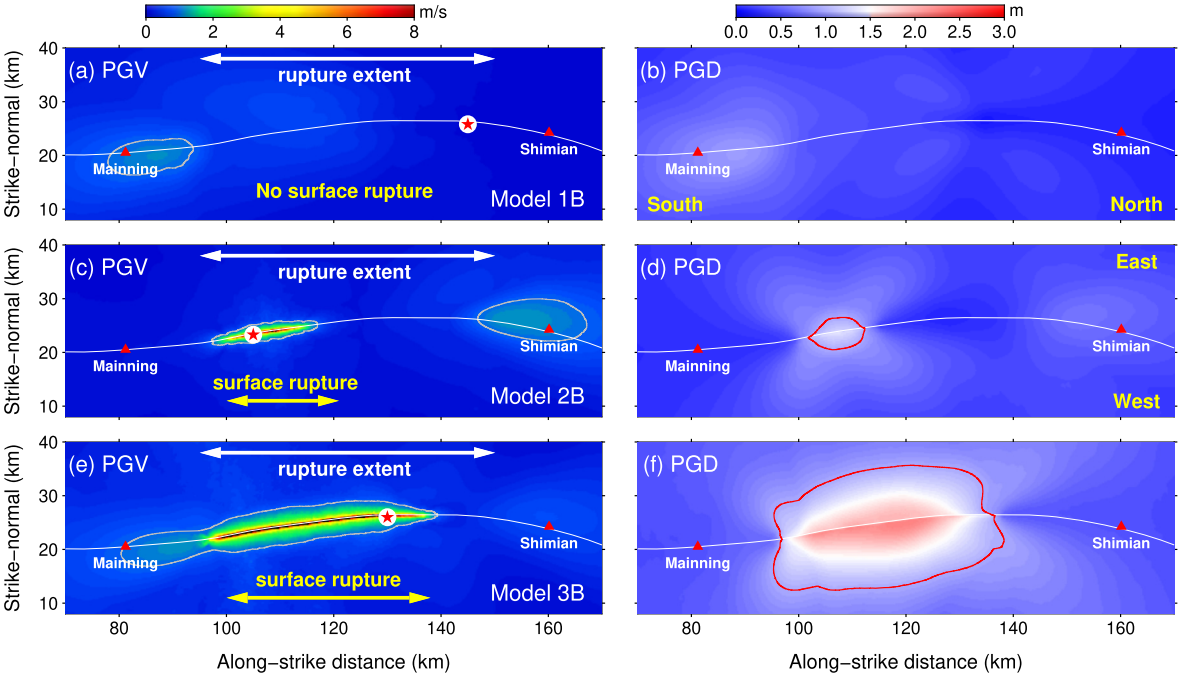

Fig. 7. Same plot with Fig. 6 but for rupture models 1B-3B in Fig. 3.

illustrate the ground shaking intensity, we calculate the intensity indexes including the peak ground velocity (PGV) and the peak ground displacement (PGD) from the synthetic waveforms. Through examining the distribution of PGV and PGD of the six models shown in Fig. 3, we find that the surface rupture and shallow slip significantly contribute to the intensity distribution by causing violent ground shaking within a short distance (∼5 km) from the fault trace (Fig. 6 & 7). If the rupture does not break the surface, both PGV and PGD are modest (Fig. 7a & 7b). In comparison, a surface-breaching rupture can generate significant strong shaking, with PGV larger than 6 m/s near the fault trace (Fig. 6e). Furthermore, a rupture without significant SSD is more destructive, as the area with large values of PGV and PGD gets larger (Fig. 7e & 7f).

In addition, the rupture directivity largely impacts ground shaking. For instance, the rupture that initiates from the southern edge of segment M3 and propagates to the north causes the smearing of the PGV pattern near where the rupture terminates (Fig. 6c & 7c). Such directivity effect is caused by the concentration of the S-wave energy radiated from the rupture front that grows with the rupture

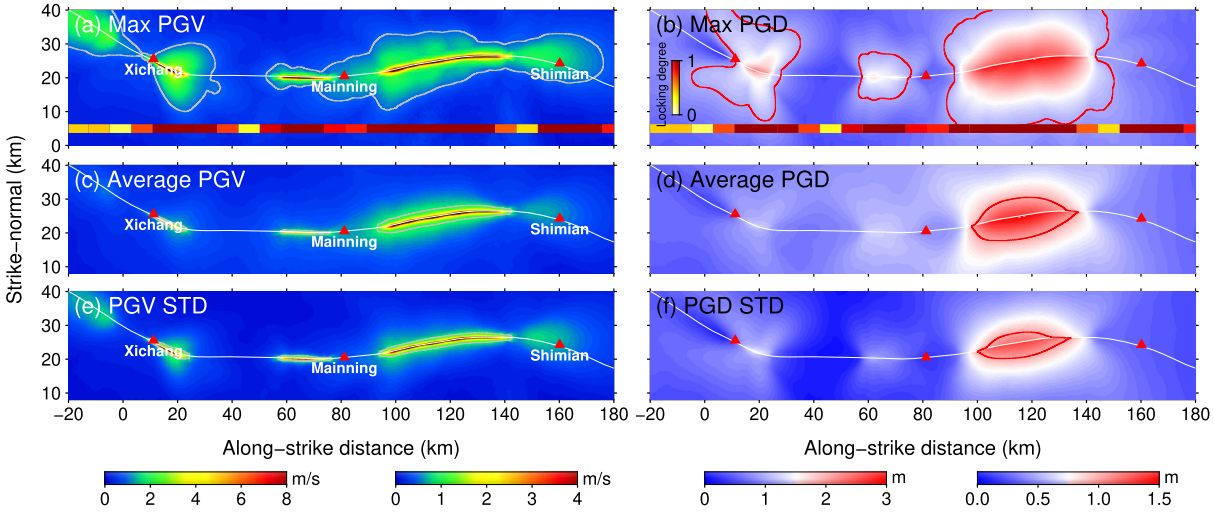

Fig. 8. (a & b) The max PGVs and PGAs among our rupture scenarios with τ_s of 60 MPa and Dc of 0.6 m. The average PGVs (c) and PGDs (d) and the respective standard deviations (e & f) among rupture scenarios. The red triangles denote the locations of cities near the Anninghe fault. The colored thick lines in (a) and (b) indicate the locking degree along the Anninghe fault (Jiang et al., 2015). The colorbars on the left under each column are applied to the peak values (a & b), while the two on the right are applied to the mean values (c & d) and the standard deviations (e & f).

propagation and attenuates outside the rupture extent (Somerville, 2005). Different from PGV, the PGD is almost solely determined by the rupture extent and surface rupture, to which the directivity effect is minor (Fig. 6d & 6f).

To better understand the seismic risk in this region, we pick the max PGV and PGD among all rupture scenarios as the indicator for the potential highest ground shaking for models with the yield stress of 60 MPa and the Dc of 0.6 m (Fig. 8a & 8b). Moreover, we calculate the mean values (Fig. 8c & 8d) and the standard deviations of predictions among models (Fig. 8e & 8f). The results indicate that the regions along the locked segments feature higher ground shaking risk compared to the creeping zones. However, the ground motions can be considerable at the gap between the segment M3 and M2 due to the strong rupture directivity effects from ruptures along the M3 segment (Fig. 8a). The ground motion predictions in our models can be used in generating future hazard maps, especially for the near-fault regions.

4.4. Segmentation and SSD in earthquake cycles

One of the basic assumptions in our models is that the pre-earthquake stress is determined by a linear stress accumulation since the last characteristic earthquake. However, it has been evidenced that the locking state on the fault may evolve over time (Bruhat and Segall, 2017). In addition, the locking model for the Anninghe fault was derived based on geodetic data with a period of ~10 years (Jiang et al., 2015), much shorter than the recurrence intervals of characteristic earthquakes along the Anninghe fault (400-600 yrs) (Wen, Ma et al., 2008). Geodetic observations with a longer observation period are required to better understand the stress evolution. Therefore, such assumptions may lead to uncertainties in estimating the slip deficit and the stress accumulation.

In addition, here we assume a uniform residual stress field after the last large event. Although characteristic earthquakes to some degree smooth the stress field, the stress patterns may evolve over earthquake cycles and lead to different segmentation patterns (Kaneko and Lapusta, 2010; Luo and Ampuero, 2018). This can be a potential explanation for why rupture through the entire southern segment of the Anninghe fault is absent in our results but was inferred to have occurred in 1536. In our models focusing on the coseismic rupture process for single events, the shallow slip deficit comes from the lack of strain energy in the shallow zone. However, with stress accumulated over earthquake cycles, the shallow slip deficit may be compensated by different events. To understand such long-term behaviors, earthquake-cycle modeling is demanded.

5. Conclusion

We derived rupture scenarios with a locking-based heterogeneous stress condition along the Anninghe fault. Our model predictions on magnitudes and rupture extents are consistent with historical events, underlining the reliability of the locking-based scenarios. In addition, we observe varying surface rupture patterns and the shallow slip that were controlled by the hypocenter locations. Since our prescribed initial conditions are identical, such hypocentral-dependent shallow slip and surface-breaching ruptures could be a viable explanation of observations. We further derive consequent ground motion intensities of all rupture scenarios, underlining the non-linear rupture process on a fault under heterogeneous stress. Now our models focus on single-event cases. Understanding the long-term behaviors of the rupture extent and the shallow slip requires further efforts on cycle modeling. Our rupture scenarios, together with the synthetic ground motions, can serve in future seismic hazard assessment, especially for near-fault regions with rare observations yet severe intensities.

CRediT authorship contribution statement

Both authors contributed in developing main ideas, interpreting the results, and producing the manuscript.

Declaration of competing interest

The authors declare that they have no known competing financial interests or personal relationships that could have appeared to influence the work reported in this paper.

Acknowledgement

This study is supported by the National Key R&D Program of China (2018YFC1503400), Hong Kong Research Grant Council Grants (14306119, 14306418), China Earthquake Science Experiment Project, CEA (grant no. 2018CSES0102), State Key Lab of

Earthquake Dynamics (grant No. LED2021B03), The Open Foundation of the United Laboratory of Numerical Earthquake Forecasting (grant No. 2021LNEF02), CUHK Direct Grant from Faculty of Science.

Appendix A. Supplementary material

Supplementary material related to this article can be found online at https://doi.org/10.1016/j.epsl.2021.117296.

References

Aagaard, B.T., Knepley, M.G., Williams, C.A., 2013. A domain decomposition approach to implementing fault slip in finite-element models of quasi-static and dynamic crustal deformation. J. Geophys. Res. 118, 3059–3079.

Ader, T., et al., 2012. Convergence rate across the Nepal Himalaya and interseismic coupling on the Main Himalayan Thrust: implications for seismic hazard. J. Geophys. Res. 117, B04403. https://doi.org/10.1029/2011JB009071.

Andrews, D.J., Ben-Zion, Y., 1997. Wrinkle-like slip pulse on a fault between different materials. J. Geophys. Res. 102 (B1), 553–571. https://doi.org/10.1029/96JB02856.

Barbot, S., Fialko, Y., Sandwell, D., 2008. Effect of a compliant fault zone on the inferred earthquake slip distribution. J. Geophys. Res. 113 (B06404).

Barbot, S., Fialko, Y., Sandwell, D., 2009. Three-dimensional models of elasto-static deformation in heterogeneous media, with application to the Eastern California Shear Zone. Geophys. J. Int. 179, 500–520.

Baranes, H., Woodruff, J.D., Loveless, J.P., Hyodo, M., 2018. Interseismic coupling-based 460 earthquake and tsunami scenarios for the Nankai Trough. Geophys. Res. Lett. 461 (45), 2986–2994. https://doi.org/10.1002/2018GL077329.

Biggs, J., Bergman, E., Emmerson, B., Funning, G.J., Jackson, J., Parsons, B., Wright, T.J., 2006. Fault identification for buried strike-slip earthquakes using InSAR: the 1994 and 2004 Al Hoceima, Morocco earthquakes. Geophys. J. Int. 166 (3), 1347–1362.

Bruhat, L., Segall, P., 2017. Deformation rates in northern Cascadia consistent with slow updip propagation of deep interseismic creep. Geophys. J. Int. 211, 427–449. https://doi.org/10.1093/gji/ggx317.

Bydlon, S.A., Withers, K.B., Dunham, E.M., 2019. Combining dynamic rupture simulations with ground-motion data to characterize seismic hazard from Mw 3 to 5.8 earthquakes in Oklahoma and Kansas. Bull. Seismol. Soc. Am. 109 (2), 652–671. https://doi.org/10.1785/0120180042.

Cocco, M., Marone, C., Tinti, E., Piatanesi, A., 2009. Scaling of slip weakening distance with final slip during dynamic earthquake rupture. In: Fukuyama, E. (Ed.), Fault-zone Properties and Earthquake Rupture Dynamics. Elsevier.

Das, S., Scholz, C.H., 1983. Why large earthquakes do not nucleate at shallow depths. Nature 305 (13), 621–623.

Deng, Q., Zhang, P., Ran, Y., Yang, Z., Min, W., Chu, Q., 2003. Basic characteristics of active tectonics of China. Sci. China, Ser. D, Earth Sci. 46, 356–372.

Di Toro, G., Han, R., Hirose, T., et al., 2011. Fault lubrication during earthquakes. Nature 471, 494–498. https://doi.org/10.1038/nature09838.

Elliott, A.J., Oskin, M.E., Liu-Zeng, J., Shao, Y., 2015. Rupture termination at restraining bends: the last great earthquake on the Altyn Tagh Fault. Geophys. Res. Lett. 42, 2164–2170. https://doi.org/10.1002/2015GL063107.

Feng, L., Newman, A.V., Protti, M., Gonzalez, V., Jiang, Y., Dixon, T.H., 2012. Active deformation near the Nicoya Peninsula, northwestern Costa Rica, between 1996 and 2010: interseismic megathrust coupling. J. Geophys. Res., Solid Earth 117, B06407.

Fialko, Y., Sandwell, D., Simons, M., Rosen, P., 2005. Three-dimensional deformation caused by the Bam, Iran, earthquake and the origin of shallow slip deficit. Nature 435, 295–299. https://doi.org/10.1038/nature03425.

Fournier, T.J., Freymueller, J.T., 2007. Transition from locked to creeping subduction in the Shumagin region, Alaska. Geophys. Res. Lett. 34, L06303. https://doi.org/10.1029/2006GL029073.

Galis, M., Pelties, C., Kristek, J., Moczo, P., Ampuero, J.-P., Mai, P.M., 2015. On the initiation of sustained slip-weakening ruptures by localized stresses. Geophys. J. Int. 200 (2), 890–909. https://doi.org/10.1093/gji/ggu436.

Gabriel, A.-A., Ampuero, J.-P., Dalguer, L.A., Mai, P.M., 2012. The transition of dynamic rupture styles in elastic media under velocity-weakening friction. J. Geophys. Res. 117, B09311. https://doi.org/10.1029/2012JB009468.

Goebel, T.H.W., Becker, T.W., Schorlemmer, D., Stanchits, S., Sammis, C., Rybacki, E., Dresen, G., 2012. Identifying fault heterogeneity through mapping spatial anomalies in acoustic emission statistics. J. Geophys. Res. 117, B03310. https://doi.org/10.1029/2011JB008763.

Harris, R.A., Barall, M., Lockner, D.A., Moore, D.E., Ponce, D.A., Graymer, R.W., Funning, G., Morrow, C.A., Kyriakopoulos, C., Eberhart-Phillips, D., 2021. A geology and geodesy based model of dynamic earthquake rupture on the Rodgers Creek-Hayward-Calaveras fault system, California. J. Geophys. Res., Solid Earth 126 (3).

Harris, R., 2004. Numerical simulations of large earthquakes: dynamic rupture propagation on heterogeneous faults. Pure Appl. Geophys. 161, 2171–2181.

Ida, Y., 1972. Cohesive force across the tip of a longitudinal-shear crack and Griffith's specific surface energy. J. Geophys. Res. 77 (20), 3796–3805.

Jiang, J., Fialko, Y., 2016. Reconciling seismicity and geodetic locking depths on the Anza section of the San Jacinto fault. Geophys. Res. Lett. 43, 10,663–10,671. https://doi.org/10.1002/2016GL071113.

Jiang, G., Xu, X., Chen, G., Liu, Y., Fukahata, Y., Wang, H., Yu, G., Tan, X., Xu, C., 2015. Geodetic imaging of potential seismogenic asperities on the Xianshuihe-Anninghe-Zemuhe fault system, southwest China, with a new 3-D viscoelastic interseismic coupling model. J. Geophys. Res., Solid Earth 120, 1855–1873. https://doi.org/10.1002/2014JB011492.

Kuo, L.-W., Li, H., Smith, S.A.F., Di Toro, G., Suppe, J., Song, S.-R., et al., 2013. Gouge graphitization and dynamic fault weakening during the 2008 Mw 7.9 Wenchuan earthquake. Geology 42 (1), 47–50. https://doi.org/10.1130/g34862.1.

Shimazaki, K., 1986. Small and large earthquakes: the effects of the thickness of seismogenic layer and the free surface. In: Das, S., Boatwright, J., Scholz, C.H. (Eds.), Earthquake Source Mechanics.

Kaneko, Y., Fialko, Y., 2011. Shallow slip deficit due to large strike-slip earthquakes in dynamic rupture simulations with elasto-plastic off-fault response. Geophys. J. Int. 186 (3), 1389–1403. https://doi.org/10.1111/j.1365-246X.2011.05117.x.

Kaneko, Y., Lapusta, N., 2010. Supershear transition due to a free surface in 3-D simulations of spontaneous dynamic rupture on vertical strike-slip faults. Tectonophysics (ISSN 0040-1951) 493 (3–4), 272–284. https://doi.org/10.1016/j.tecto.2010.06.015.

King, G., Nábělek, J., 1985. Role of fault bends in the initiation and termination of earthquake rupture. Science 228, 984–987.

Lei, J., Zhao, D., 2009. Structural heterogeneity of the Longmenshan fault zone and the mechanism of the 2008 Wenchuan earthquake (Ms 8.0). Geochem. Geophys. Geosyst. 10, Q10010. https://doi.org/10.1029/2009GC002590.

Li, Y., Song, X., Shan, X., Qu, C., Wang, Z., 2016. Locking degree and slip rate deficit distribution on MHT fault before 2015 Nepal Mw 7.9 earthquake. J. Asian Earth Sci. (ISSN 1367-9120) 119, 78–86. https://doi.org/10.1016/j.jseaes.2016.01.011.

Li, D., Liu, Y., 2021. Cascadia megathrust earthquake rupture model constrained by geodetic fault locking. Philos. Trans. R. Soc. A, Math. Phys. Eng. Sci. 379 (2196), 20200135.

Lindsey, E.O., Fialko, Y., 2013. Geodetic slip rates in the southern San Andreas Fault system: effects of elastic heterogeneity and fault geometry. J. Geophys. Res., Solid Earth 118, 689–697. https://doi.org/10.1029/2012JB009358.

Luo, Y., Ampuero, J-P., 2018. Stability of faults with heterogeneous friction properties and effective normal stress. Tectonophysics (ISSN 0040-1951) 733, 257–272. https://doi.org/10.1016/j.tecto.2017.11.006.

McCaffrey, R., 2014. Interseismic locking on the Hikurangi subduction zone: uncertainties from slow-slip events. J. Geophys. Res., Solid Earth 119, 7874–7888. https://doi.org/10.1002/2014JB010945.

Moreno, M., Rosenau, M., Oncken, O., 2010. Maule earthquake slip correlates with pre-seismic locking of Andean subduction zone. Nature 467 (7312), 198–202.

Nielsen, S., Spagnuolo, E., Smith, S.A.F., Violay, M., Di Toro, G., Bistacchi, A., 2016. Scaling in natural and laboratory earthquakes. Geophys. Res. Lett. 43, 1504–1510. https://doi.org/10.1002/2015GL067490.

Noda, A., Saito, T., Fukuyama, E., Urata, Y., 2021. Energy-based scenarios for great thrust-type earthquakes in the Nankai trough subduction zone, Southwest Japan, using an interseismic slip-deficit model. J. Geophys. Res., Solid Earth 126 (5), e2020JB020417.

Noda, A., Saito, T., Fukuyama, E., 2018. Slip-deficit rate distribution along the Nankai trough, Southwest Japan, with elastic lithosphere and viscoelastic asthenosphere. J. Geophys. Res., Solid Earth 123, 8125–8142. https://doi.org/10.1029/2018jb015515.

Olsen, K.B., Day, S.M., Minster, J.B., Cui, Y., Chourasia, A., Faerman, M., Moore, R., Maechling, P., Jordan, T.H., 2006. Strong shaking in Los Angeles expected from southern San Andreas earthquake. Geophys. Res. Lett. 33, L07305. https://doi.org/10.1029/2002JB002235.

Pitarka, A., Dalguer, L.A., Day, S.M., Somerville, Paul G., Dan, Kazuo, 2009. Numerical study of ground-motion differences between buried-rupturing and surface-rupturing earthquakes. Bull. Seismol. Soc. Am. 99 (3), 1521–1537. https://doi.org/10.1785/0120080193.

Protti, M., González, V., Newman, A.V., Dixon, T.H., Schwartz, S.Y., Marshall, J.S., Feng, L., Walter, J.I., Malservisi, R., Owen, S.E., 2014. Nicoya earthquake rupture anticipated by geodetic measurement of the locked plate interface. Nat. Geosci. 7 (2), 117–121.

Ran, Y., Chen, L., Cheng, J., Gong, H., 2008. Late Quaternary surface deformation and rupture behavior of strong earthquake on the segment north of Mianning of the Anninghe fault. Sci. China, Ser. D, Earth Sci. 51, 1224–1237.

Rice, J.R., 2006. Heating and weakening of faults during earthquake slip. J. Geophys. Res. 111, B05311.

Ripperger, J., Mai, P.M., Ampuero, J.P., 2008. Variability of near-field ground motion from dynamic earthquake rupture simulations. Bull. Seismol. Soc. Am. 98 (3), 1207–1228. https://doi.org/10.1785/0120070076.

Ramos, M.D., Huang, Y., Ulrich, T., Li, D., Gabriel, A.A., Thomas, A.M., 2021. Assessing margin-wide rupture behaviors along the Cascadia megathrust with 3-D dynamic rupture simulations. J. Geophys. Res., Solid Earth, e2021JB022005.

Roten, D., Olsen, K.B., Day, S.M., 2017. Off-fault deformations and shallow slip deficit from dynamic rupture simulations with fault zone plasticity. Geophys. Res. Lett. https://doi.org/10.1002/2017GL074323.

Shrivastava, M.N., González, G., Moreno, M., Chlieh, M., Salazar, P., Reddy, C.D., et al., 2016. Coseismic slip and afterslip of the 2015 M_w 8.3 Illapel (Chile) earthquake determined from continuous GPS data. Geophys. Res. Lett. 43, 10,710–10,719. https://doi.org/10.1002/2016GL070684.

Somerville, P.G., 2005. Engineering characterization of near fault ground motion. In: 2005 New Zealand Society for Earthquake Engineering Conference. Taupo, New Zealand. 8 pp.

Tymofyeyeva, E., Fialko, Y., 2018. Geodetic evidence for a blind fault segment at the southern end of the San Jacinto Fault Zone. J. Geophys. Res., Solid Earth 123, 878–891. https://doi.org/10.1002/2017JB014477.

Viesca, R.C., Garagash, D.I., 2015. Ubiquitous weakening of faults due to thermal pressurization. Nat. Geosci. 8 (11), 875–879. https://doi.org/10.1038/ngeo2554.

Wen, X., Du, P., Long, D., 2000. New evidence of paleoearthquakes and date of the latest event on the Xiaoxiangling mountain segment of the Anninghe fault zone. Seismol. Geol. 22, 1–8 (in Chinese).

Wen, X., Fan, J., Yi, G., Deng, Y., Long, F., 2008. A seismic gap on the Anninghe fault in western Sichuan, China. Sci. China, Ser. D, Earth Sci. 51 (10), 1375–1387.

Wen, X., Ma, S., Lei, X., Kuwahara, Y., Kiguchi, T., Chen, Q., 2007. Newly found surface rupture remains of large historical earthquakes on and near the transition segment of the Anninghe and Zemuhe fault zones, western Sichuan, China. Seismol. Geol. 29, 826–833 (in Chinese).

Wen, X., Ma, S., Xu, X., He, Y., 2008. Historical pattern and behavior of earthquake ruptures along the eastern boundary of the Sichuan-Yunnan faulted block, southwestern China. Phys. Earth Planet. Inter. 168, 16–36.

Weng, H., Yang, H., 2018. Constraining frictional properties on fault by dynamic rupture simulations and near-field observations. J. Geophys. Res. https://doi.org/10.1029/2017JB015414.

Weng, H., Yang, H., Zhang, Z., Chen, X., 2016. Earthquake rupture extents and coseismic slips promoted by damaged fault zones. J. Geophys. Res., Solid Earth 121, 4446–4457.

Wyss, M., 2001. Locked and creeping patches along the Hayward Fault, California. Geophys. Res. Lett. 28, 3537–3540. https://doi.org/10.1029/2001GL013499.

Xu, C., Liu, Y., Wen, Y., Wang, R., 2010. Coseismic slip distribution of the 2008 M_w 7.9 Wenchuan earthquake from joint inversion of GPS and InSAR data. Bull. Seismol. Soc. Am. 100 (5B), 2736–2749. https://doi.org/10.1785/0120090253.

Xu, J., Zhang, H., Chen, X., 2015. Rupture phase diagrams for a planar fault in 3-D full-space and half-space. Geophys. J. Int. 202 (3), 2194–2206. https://doi.org/10.1093/gji/ggv284.

Xu, X., Tong, X., Sandwell, D., Milliner, Christopher W.D., Dolan, James F., Hollingsworth, James, Leprince, Sebastien, Ayoub, Francois, 2016. Refining the shallow slip deficit. Geophys. J. Int. 204 (3), 1867–1886. https://doi.org/10.1093/gji/ggv563.

Yang, H., Yao, S., 2021. Shallow destructive earthquakes. Earthq. Sci. 34 (1). https://doi.org/10.29382/eqs-2020-0072.

Yang, H., Liu, Y., Lin, J., 2012. Effects of subducted seamounts on megathrust earthquake nucleation and rupture propagation. Geophys. Res. Lett. 39, L24302. https://doi.org/10.1029/2012GL053892.

Yang, H., Liu, Y., Lin, J., 2013. Geometrical effects of a subducted seamount on stopping megathrust ruptures. Geophys. Res. Lett. 40, 1–6. https://doi.org/10.1002/grl.50509.

Yang, H., Yao, S., He, B., Newman, A.V., 2019b. Earthquake rupture dependence on hypocentral location along the Nicoya Peninsula subduction megathrust. Earth Planet. Sci. Lett. 520, 10–17. https://doi.org/10.1016/j.epsl.2019.05.030.

Yang, H., Yao, S., He, B., Newman, A.V., Weng, H., 2019a. Deriving rupture scenarios from interseismic locking distributions along the subduction megathrust. J. Geophys. Res. 124, 10376–10392. https://doi.org/10.1029/2019JB017541.

Yang, H., Zhu, L., Cochran, E.S., 2011. Seismic structures of the Calico fault zone inferred from local earthquake travel time modelling. Geophys. J. Int. 186 (2), 760–770. https://doi.org/10.1111/j.1365-246X.2011.05055.x.

Yang, Y., Yao, H., Wu, H., Zhang, P., Wang, M., 2020. A new crustal shear-velocity model in Southwest China from joint seismological inversion and its implications for regional crustal dynamics. Geophys. J. Int. 220 (2), 1379–1393. https://doi.org/10.1093/gji/ggz514.

Yang, Z., Wang, F., Duan, Y., Zhang, C., Zhao, J., Zhang, J., Liu, B., 2011. Basement structure of southeastern boundary region of Sichuan-Yunnan active blocks: analysis result of Yanyuan-Xichang-Zhaojue-Mahu deep seismic sounding profile [in Chinese with English abstract]. Acta Seismol. Sin. 33 (4), 431–442.

Yao, L., Ma, S., Shimamoto, Toshihiko, Togo, Tetsuhiro, 2013. Structures and high-velocity frictional properties of the Pingxi fault zone in the Longmenshan fault system, Sichuan, China, activated during the 2008 Wenchuan earthquake. Tectonophysics (ISSN 0040-1951) 599, 135–156. https://doi.org/10.1016/j.tecto.2013.04.011.

Yao, S., Yang, H., 2020. Rupture dynamics of the 2012 Nicoya Mw 7.6 earthquake: evidence for low strength on the megathrust. Geophys. Res. Lett. 47, e2020GL087508. https://doi.org/10.1029/2020GL087508.

Yu, W., Song, F., Wen, X., Li, C., 2001. Study of the surface rupture zone of the Xichang earthquake in 1850. J. Seismol. Res. 24, 346–350 (in Chinese).